

Thermal response functions and second sound in graphene

Antonio Martinez Margolles¹ and Patrick K. Schelling^{1,2}

¹*Department of Physics, University of Central Florida, Orlando, FL 32816-2385, USA*

²*Advanced Materials Processing and Analysis Center, University of Central Florida, Orlando, FL 32816-2385, USA*

December 17, 2025

Abstract

The propagation of second sound, and more broadly the ballistic transport of heat, is of central importance in heat dissipation from electronic devices at very short length and time scales. Specifically, there is an interest in the practical implications of violations of Fourier's law. Recently, we have developed a simulation approach based on thermal-response functions that is appropriate for elucidating physics beyond the diffusive regime, including time-dependent sources and second-sound propagation. The methods are applied to free-standing graphene simulated using molecular-dynamics (MD) with empirical potentials. The simulations predict a strong second-sound signal at $T = 300\text{K}$ for length scales of at least $L = 68.1\text{nm}$. It is demonstrated that the second-sound dissipation time is determined primarily by decoherence that emerges from the details of the phonon band structure. It is also shown that the decay time for second sound depends sensitively on the length scale that characterizes the thermal excitation. This is in contrast with theories based on the Boltzmann transport equation (BTE), where second-sound dissipation is determined primarily by the resistive anharmonic phonon scattering rate, which is independent of length scale. Calculations using the linearized Boltzmann transport equation (LBTE) are also presented, along with analysis of second sound based on the single-mode relaxation time approximation (SMA). This approach, consistent with previous authors, results in significantly longer lifetimes for second sound in comparison to our MD simulation results. Predictions for the response due to time-dependent sources are also presented, including insight into how time-dependent sources could be tuned to result in weak or strong temperature oscillations, and how time-dependent experiments might probe the spectra associated with second sound. Finally, results are discussed in the context of recent observations of second sound in graphite crystals in the temperature range from 100 – 200K.

1 Introduction

Recent experiments using transient-thermal grating (TTG) techniques have demonstrated the presence of second-sound propagation in graphite [1, 2] at temperatures over 200K. The relevance of this transport mechanism to applications is established by the fact that it was observed for grating periods of about $2\mu\text{m}$. Moreover, theoretical calculations of graphene have established that boundary scattering effects are dominant at scales $\sim 1\mu\text{m}$ [3] which substantiates the relevance of ballistic transport to potential device applications. Despite these facts, the vast majority of theoretical calculations are focused on computing thermal conductivity κ , which presume the relevance of the heat-diffusion equation, and hence are not relevant for transport via second sound. More broadly, most approaches are insufficient for a description of time-dependent heat sources when Fourier's law does not apply.

The phenomenological description of second sound has been based on the hyperbolic heat equation for the evolution of the temperature field $T(\mathbf{r}, t)$,

$$\frac{\partial^2 T(\mathbf{r}, t)}{\partial t^2} + \frac{1}{\tau_{ss}} \frac{\partial T(\mathbf{r}, t)}{\partial t} - v_{ss}^2 \nabla^2 T(\mathbf{r}, t) = 0. \quad (1)$$

This equation, written in Fourier space, with $T_{\mathbf{q}}(t)$ representing a deviation from equilibrium with wave vector \mathbf{q} , is described by the damped oscillator equation,

$$\frac{d^2 T_{\mathbf{q}}}{dt^2} + \frac{1}{\tau_{ss}} \frac{dT_{\mathbf{q}}}{dt} + q^2 v_{ss}^2 T_{\mathbf{q}} = 0, \quad (2)$$

in which $q^2 = \mathbf{q} \cdot \mathbf{q}$. Hence, perhaps more specifically, oscillations in the temperature field can be observed when $\tau_{ss} > \frac{1}{2qv_{ss}}$. Because τ_{ss} and v_{ss} represent the lifetime and propagation velocity of temperature waves, this is simply stating that τ_{ss} must be large enough to encompass at least one period of oscillation for wave behavior to be observed. If $\tau_{ss} < \frac{1}{2qv_{ss}}$, a temperature deviation $T_{\mathbf{q}}(t)$ will simply exponentially decay with time. Finally, if $\tau_{ss} \ll \frac{1}{2qv_{ss}}$, eventually Fourier's law behavior is expected to apply. It is standard to use solutions to the BTE to predict values for v_{ss} and τ_{ss} [4, 5]. More recently, theoretical predictions have been grounded in first-principles calculations typically using Density-Functional Theory (DFT) [6–10].

In this paper, we apply our recently-developed [11–13] approach using classical molecular-dynamics (MD) simulation to compute the thermal-response functions for graphene at $T = 300\text{K}$. The advantage of this approach is that it makes predictions without any assumptions about whether transport is diffusive or ballistic, and moreover is directly comparable to experiments using TTG techniques. In previous works, response functions were able to identify the presence of second sound in one-dimensional chains [12] and hBN monolayers [13]. Here we demonstrate the presence of second sound in graphene at $T = 300\text{K}$ over length scales up to $L = 68.1\text{nm}$. The phenomenological expression in Eq. 2 is compared to the MD simulations to obtain values for τ_{ss} and v_{ss} . This is then compared to predictions based on density-functional theory (DFT) calculations and theoretical expressions for second-sound based on Ref. [7]. It will be shown, in contrast to the assumptions made by BTE-based theories of second sound, that τ_{ss} strongly depends on the wave vector \mathbf{q} of the perturbation. Moreover, it will be demonstrated that the primary mechanism for the decay in the second sound signal at $T = 300\text{K}$ at these length scales is the loss of phase coherence due to normal-mode dispersion rather than anharmonic scattering. Specifically, an external heat pulse like those generated in a TTG experiment generates phase coherence between normal modes which is lost as different modes in the wave propagate at different velocities. Comparison to experimental TTG techniques applied to graphite appear to follow this qualitative picture [2]. At short length scales (i.e. the grating period), this mechanism leads to values for τ_{ss} which are much smaller than those obtained from BTE theories. Finally, we examine the physics of time-dependent perturbations, which is used to develop insight into how time-dependent sources could be used to probe the spectra of second sound.

2 Approach: Classical MD

The interactions to describe graphene are taken from the optimized Tersoff potential reported in Ref. [14]. As with our previous study [13], the expressions for heat current due to Fan and coworkers [15] were used. The thermal conductivity κ was computed according to the Green-Kubo expression,

$$\kappa(\tau) = \frac{\Omega}{3k_B T^2} \int_0^\tau \langle \mathbf{J}(t) \cdot \mathbf{J}(0) \rangle dt \quad (3)$$

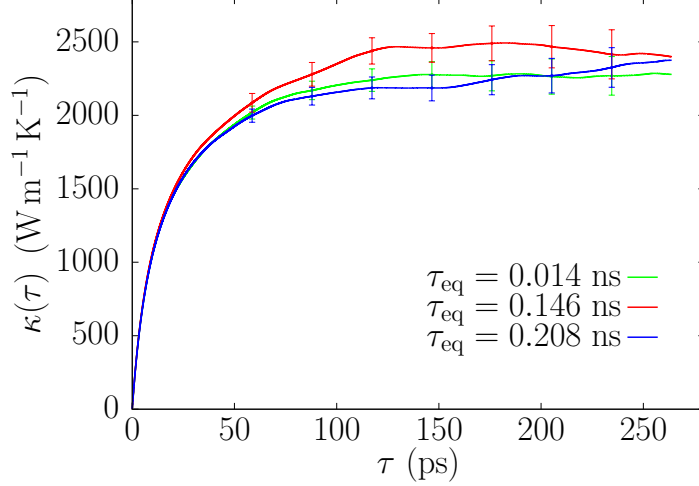


Figure 1: Thermal conductivity integral in Eq. 3 plotted as a function of the upper integration limit τ for different equilibration times τ_{eq} .

with the thermal conductivity formally given by taking the limit $\kappa = \lim_{\tau \rightarrow \infty} \kappa(\tau)$. To define the system volume Ω for the two-dimensional system, the layer spacing in graphite $c = 3.35\text{\AA}$ was used. For the in-plane directions, the lattice parameters were chosen to result in $T = 0\text{K}$ C-C bond length of 1.44\AA , which is fairly close to the zero-stress result in Ref. [14], but slightly expanded from the experimental value $\sim 1.42\text{\AA}$. All simulations were conducted at constant volume, and hence at $T = 300\text{K}$, the system is under tensile stress since thermal contraction cannot occur. Accurate calculation of κ requires thermal equilibration of the simulated system and large amounts of simulation data for statistical averaging. We used an ensemble of 640 independent calculations each with 0.292 ns of simulation data within the constant energy and volume ensemble to compute the time-averaged current-current correlation function. Hence, the total amount of simulation time used for averaging was 186.9 ns. The time step for integration of the equations of motion was 0.146 fs which was small enough to demonstrate excellent energy conservation. Finally, the system was chosen to have dimensions 320×32 cells along the \mathbf{a}_1 and \mathbf{a}_2 lattice vectors. Hence the system size comprised $N = 20,480$ atoms. The supercell was chosen in this way such that coherent wave-like transport could be examined over long length scales without excessive computational cost. The supercell used was $L = 68.1$ nm along the long direction.

In addition to requiring a large statistical ensemble, the calculation of κ may depend somewhat on the initial equilibration period under the action of the thermostat. Each of the 640 simulations in the ensemble was preceded by an independent, constant temperature equilibration period. In Fig. 1, the value of $\kappa(\tau)$ is shown as a function of the upper limit of integration τ for three different equilibration times. The error bars in Fig. 1 represent the standard deviation determined over the entire ensemble. While there does appear to be some weak dependence on τ_{eq} , for $\tau_{eq} = 0.146\text{ns}$ and $\tau_{eq} = 0.208\text{ns}$, the results agree to within the statistical uncertainty indicated by the error bars. For calculation of response functions, it will be demonstrated that the results involve shorter time scales and are even less clearly dependent on τ_{eq} . In the following, $\tau_{eq} = 0.208\text{ns}$ was used for all reported data.

The room-temperature thermal conductivity calculated using Eq. 3 in this work is 2370 ± 150 W/mK. Using the same optimized Tersoff potential, Fan reported a κ value of 2700 ± 80 W/mK in Ref. [15]. While these results are comparable, one possible reason for the disagreement might be the high aspect ratio of our simulation supercell in comparison to the supercell structures used

by Fan [15]. The calculated κ in this paper agrees well with $\kappa \approx 2300$ W/mK obtained using the same Tersoff potential with non-equilibrium MD simulation (NEMD) by Xu [27]. Other results by Haskins in Ref. [28] calculate values of κ around 2600 W/mK using an Einstein relation and MD simulation. The κ result given here is also comparable to experimental value $\kappa \approx 2500 \pm 1000$ W/mK at 350 K obtained from Raman spectroscopy of suspended CVD grown graphene [29].

The main focus of this paper is the computation of thermal response-functions which were first described in Ref [11]. The basic idea is to start from the perspective that an externally-input power density $H^{(ext)}(\mathbf{r}', t')$ will result in a subsequent heat-current density $J_\mu(\mathbf{r}, t)$ according to,

$$J_\mu(\mathbf{r}, t) = -\frac{1}{C_V} \int_{-\infty}^t dt' \int_{\Omega} d^3r' K_{\mu\mu}(\mathbf{r} - \mathbf{r}', t - t') \frac{\partial H^{(ext)}(\mathbf{r}', t')}{\partial r'_\mu}, \quad (4)$$

which assumes linear response, but crucially does not assume diffusive transport. Here, the subscript μ refers to a Cartesian component, and the expression in Eq. 4 assumes that the axes are chosen to reflect the crystal symmetry such that the input energy gradient results in a current along the same Cartesian direction μ . If the Cartesian axes are not chosen in this way, then the response function tensor \mathbf{K} will have non-zero off-diagonal components. Finally, in Eq. 4, C_V is the system heat capacity and Ω is the system volume. In the case of a two-dimensional system like graphene, Ω includes the graphite layer spacing, just as with the Green-Kubo calculations of κ described earlier.

In a periodic system, it is possible to write Eq. 4 entirely in Fourier space. We additionally take the external heat source to be a pulse at $t' = 0$ represented by, $H_q^{(ext)}(t') = u_q^{(ext)}(0)\delta(t')$. Then, with the assumption that the system is in equilibrium before the heat pulse, we can express the resulting current as,

$$J_q(t) = -\frac{i}{c_V} q K_q(t) u_q^{(ext)}(0) \quad (5)$$

in which $c_V = \frac{C_V}{\Omega}$ is the volumetric specific heat capacity and q is the magnitude of the vector $\mathbf{q} = q\hat{e}_\mu$. In practical MD calculations using periodic-boundary conditions, the possible vectors \mathbf{q} must correspond to reciprocal-lattice vectors for the simulation supercell.

Following the arguments in Ref. [11] and Ref. [13], we can determine the response function by computing the dissipation of thermal fluctuations within the equilibrium ensemble. The response function can be determined for a particular \mathbf{q} vector from,

$$K_q(\tau) = c_V \frac{\int_0^\tau dt \langle J_q(t) J_{-q}(0) \rangle}{\langle u_q(0) u_{-q}(0) \rangle} \quad (6)$$

To compute the Fourier components J_q , we require as a starting point a local definition for the heat current, which is also directly related to the Fourier components u_q of the thermal energy density. These details were presented previously in Ref. [13]. Finally, the approach here ignores “convective” terms in the definitions, which are generally understood to be unimportant for heat transport in crystalline systems.

Response functions that presume the validity of Fourier’s law and the heat-diffusion equation are easily established as Green’s functions. Specifically, assuming the validity of the heat-diffusion equation, it can be shown that $K_q(\tau) = \kappa e^{-\alpha q^2 \tau}$. Here κ is the thermal conductivity and $\alpha = \frac{\kappa}{c_V}$ is the thermal diffusivity. This provides a basis to establish deviations from the heat-diffusion equation.

3 Results: Thermal Response Functions

In the following, the data was obtained from the same ensemble of $T = 300$ K simulations for graphene. As mentioned earlier, the choice of a system with dimensions 320×32 primitive cells

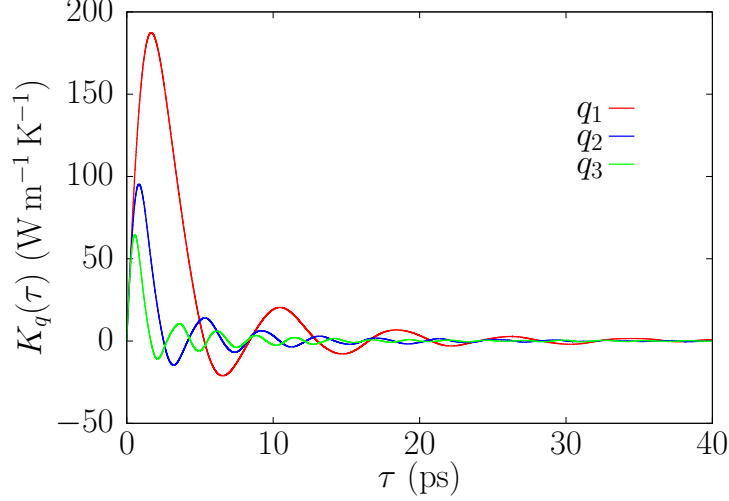


Figure 2: Response function $K_q(\tau)$ plotted as a function of time for three different wave vectors with magnitudes $q_1 = \frac{2\pi}{L}$, $q_2 = \frac{4\pi}{L}$, and $q_3 = \frac{6\pi}{L}$. As described in the text, the length scale is $L = 68.1\text{nm}$.

was made so that transport could be studied for fairly small values $q = |\mathbf{q}|$ while keeping the computational cost moderate. Given the weak dependence on τ_{eq} found in Fig. 1, we used the data obtained from $\tau_{eq} = 0.208\text{ ns}$ which appears well converged. In the following, we will also show directly that the results are very weakly dependent on τ_{eq} .

In Fig. 2, we show the computed $K_q(\tau)$ at $T = 300\text{K}$ for three different values of the wave vector, specifically $q_1 = \frac{2\pi}{L}$, $q_2 = \frac{4\pi}{L}$, and $q_3 = \frac{6\pi}{L}$ with $L = 68.1\text{nm}$ as the long dimension of the supercell. These results demonstrate very clear second-sound propagation. For example, with $q_1 = \frac{2\pi}{L}$, at least four oscillation periods are clearly discernable. For larger magnitudes q_2 and q_3 , the oscillation period and decay time both decrease. We will return to these observations later on.

To identify spectral features connected to the normal modes, we next turn to the Fourier transform of the response function,

$$\tilde{K}_q(\omega) = \int_0^{\tau_m} K_q(\tau) e^{i\omega\tau} d\tau. \quad (7)$$

Here the upper limit of integration $\tau_m = 0.292\text{ns}$ is the maximum time for each member of the simulation ensemble. This time primarily limits the resolution of the Fourier transform to $3.4 \times 10^{-3}\text{THz}$. While $K_q(\tau)$ is a real function, the Fourier transform results in real and imaginary components $K'_q(\omega)$ and $K''_q(\omega)$ respectively so that $\tilde{K}_q(\omega) = K'_q(\omega) + iK''_q(\omega)$. In Fig. 3-4, we show, respectively, the resulting data for $K''_q(\omega)$ and $K'_q(\omega)$. Along with the simulated data, the corresponding curves for Fourier's law and the heat diffusion equation using the simulated values of κ and α are also presented. First, strong disagreement between the simulation results and the heat diffusion equation is immediately evident. In our previous studies of Lennard-Jones solids [11] and hBN [13], we demonstrated that simulation results tend to converge towards the heat diffusion equation as q decreases and/or temperature increases. Next, we note that for $K''_q(\omega)$, the peaks occur near $\frac{\omega}{2\pi} = \pm 0.12\text{ THz}$. This is in agreement with the oscillations in Fig. 2 for q_1 , which appear to have a period $\tau \approx 8\text{ps}$. Second, the width of the peaks in Fig. 3 is $\sim 0.10\text{THz}$, which would correspond roughly to a lifetime of $\sim 5\text{ps}$. This quite short lifetime is consistent with the relatively strong damping of the oscillations in Fig. 2. Note that $K''_q(\omega)$ is appropriate for this

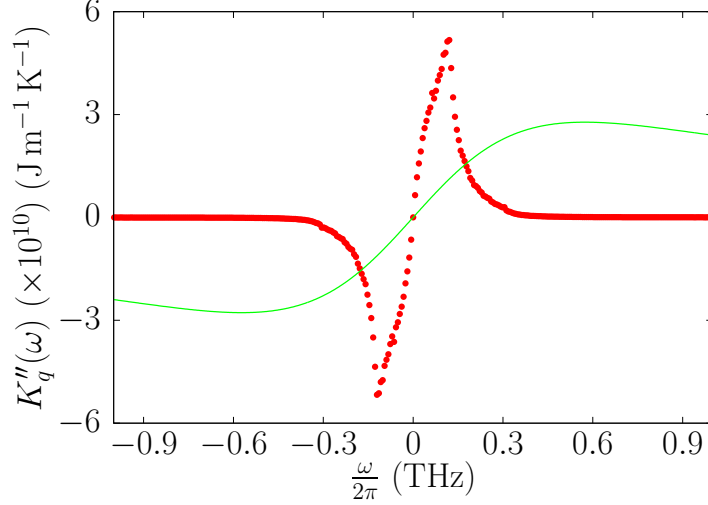


Figure 3: Imaginary part $K''_q(\omega)$ of the Fourier transformed response function plotted as a function of frequency $\frac{\omega}{2\pi}$ for $q_1 = \frac{2\pi}{L}$. The green curve shows the predicted curve based on Fourier's law using the classical heat capacity and computed thermal conductivity values κ .

analysis since $K_q(\tau)$ is best described as a damped function $\sin(\omega\tau)$ curve. Further analysis in the context of the hyperbolic heat equation will follow later.

From our previous work [13], it is clear that larger magnitudes of the wave vector q lead to a broader frequency range for the response and also sharper spectral features. Because the response is spread over a larger range of frequencies, sharp spectral features require less resolution to observe, and are also not as limited by finite phonon lifetimes and anharmonic phonon scattering. In Fig. 5 and 6, results for $K''_q(\omega)$ and $K'_q(\omega)$ are shown to compare the spectra for each value $q_1 = \frac{2\pi}{L}$, $q_2 = \frac{4\pi}{L}$, and $q_3 = \frac{6\pi}{L}$. These general trends are as expected based on our understanding. Specifically, detailed interpretation of the results in terms of the phonon band structure will follow. In comparison to the results for hBN [13], there are fewer sharp spectral features here. However, the hBN results which exhibited very sharp, detailed spectra were obtained at temperatures as low as $T = 100\text{K}$ and for significantly shorter length scales.

As in our previous study, the response in frequency space can be largely understood from the phonon band structure. In Fig. 7, the computed band structure for the optimized Tersoff model [14] is shown. The data was generated using the phono3py software package [16, 17] using calculated forces obtained from the empirical potential. In our previous articles [12, 13], we have demonstrated that for an excitation with wave vector q , the response is characterized by “beating” with frequencies $\pm \left(\omega_{\mathbf{k}+\frac{q}{2},s} - \omega_{-\mathbf{k}+\frac{q}{2},s} \right)$ primarily within the same band s . This insight arises from the expression for J_q derived in Ref. [13]

$$J_q = \frac{1}{2\Omega} \sum_{\mathbf{k},s} \hbar \omega_{\mathbf{k},s} v_{\mathbf{k},s} A_{\mathbf{k}+\frac{q}{2},s} B_{-\mathbf{k}+\frac{q}{2},s} . \quad (8)$$

This expression was also derived by Hardy [18]. Here, the $A_{\mathbf{k}+\frac{q}{2},s}$ and $B_{-\mathbf{k}+\frac{q}{2},s}$ represent normal-mode coordinates that can be written, in a quantum-mechanical picture, in terms of phonon creation and annihilation operators. In a band with nearly linear dispersion, with \mathbf{k} parallel to q , we expect resonant behavior across a band with $\omega_{\mathbf{k}+\frac{q}{2},s} - \omega_{-\mathbf{k}+\frac{q}{2},s} \approx \pm \omega_{q,s}$. This allows a determination of where different phonon branches should contribute to $K''_q(\omega)$. Hence the phonon spectra can be used to explain both the position of the maxima and the width of the $K''_q(\omega)$ in frequency space.

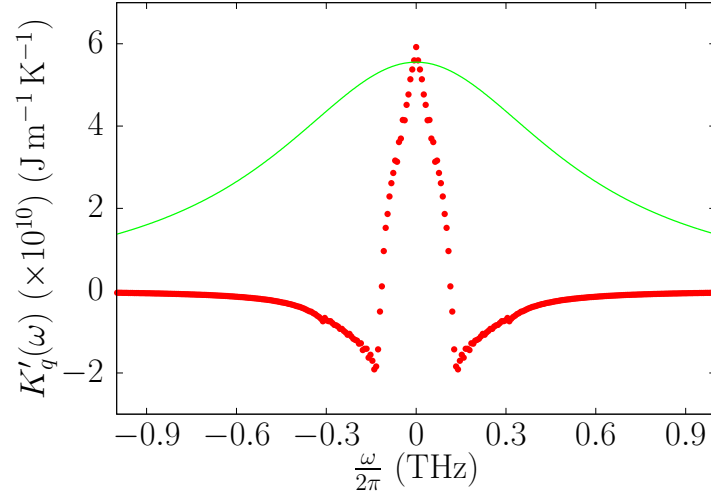


Figure 4: Real part $K'_q(\omega)$ of the Fourier transformed response function plotted as a function of frequency $\frac{\omega}{2\pi}$ for $q_1 = \frac{2\pi}{L}$. The green curve shows the predicted curve based on Fourier's law using the classical heat capacity and computed thermal conductivity values κ .

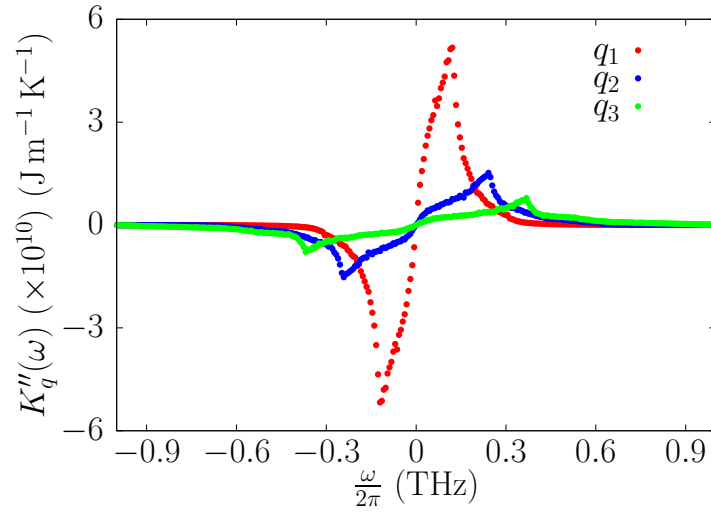


Figure 5: Imaginary component $K''_q(\omega)$ plotted as a function of time for three different wave vectors with magnitudes $q_1 = \frac{2\pi}{L}$, $q_2 = \frac{4\pi}{L}$, $q_3 = \frac{6\pi}{L}$ with $L = 68.1\text{nm}$.

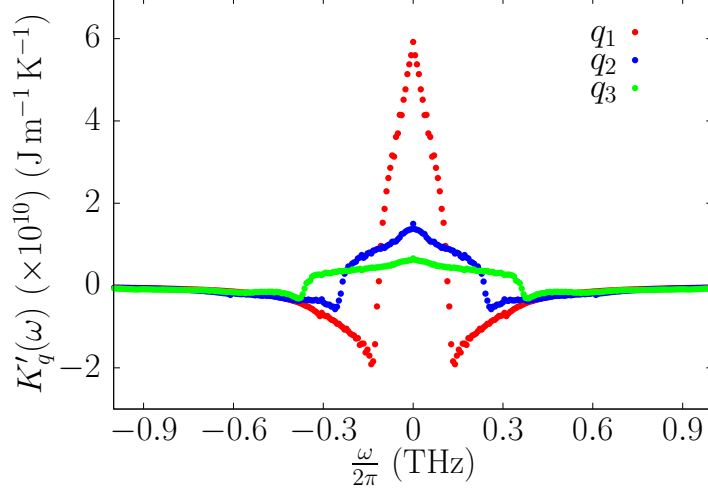


Figure 6: Real component $K'_q(\omega)$ plotted as a function of time for three different wave vectors with magnitudes $q_1 = \frac{2\pi}{L}$, $q_2 = \frac{4\pi}{L}$, $q_3 = \frac{6\pi}{L}$ with $L = 68.1\text{nm}$.

Given this insight, it is possible to identify the primary normal modes that contribute at different frequencies. For simplicity, the focus here is on interpretation of $K'_q(\omega)$, although the same considerations apply to $K''_q(\omega)$. Analysis of the band structure in Fig. 7 yields propagation speeds $v_{LA} \approx 20.3 \text{ km s}^{-1}$ and $v_{TA} \approx 14.6 \text{ km s}^{-1}$ for the longitudinal acoustic (LA) and transverse acoustic (TA) branches, respectively. For the parabolic ZA branch, v_{ZA} approaches zero at the Γ point, and has a maximum value $\sim 8 \text{ km s}^{-1}$. In the case of LA and TA modes with linear dispersion, the maximum frequencies that contribute to the response function can be determined. For $q_1 = \frac{2\pi}{L}$, the prediction is for response at a maximum frequency $\sim 0.30 \text{ THz}$ due to the LA branch, which is quite close to a small peak visible at 0.31 THz . For TA contributions, the maximum frequency is predicted to be $\sim 0.22 \text{ THz}$. The large peak in the response that occurs at $\sim 0.12 \text{ THz}$ is therefore primarily attributable to the ZA branches which should contribute significantly in the range $0 - 0.16 \text{ THz}$. However, optical modes and also other acoustic modes propagating with \mathbf{k} with a component perpendicular to \mathbf{q} also contribute. These considerations work equally well for q_2 and q_3 data at shorter length scales.

Finally, to establish that the results above are independent of τ_{eq} , the simulated equilibration time, we show in Fig. 8 results for $K''_q(\omega)$ for $q_1 = \frac{2\pi}{L}$ for each of the three values of τ_{eq} . As the figure demonstrates, the results are essentially independent of τ_{eq} . This justifies the use of $\tau_{eq} = 0.208\text{ns}$ results for the analysis above.

4 Analysis

We next apply the expression in Eq. 2 to the response-function data to obtain values for τ_{ss} and v_{ss} that best fit the simulation data. Moreover, here we will develop the equation for evolution of the temperature field that can be directly compared to experiments using TTG techniques. Assuming that Eq. 2 is in the underdamped regime where $\tau_{ss} < \frac{1}{2qv_{ss}}$, the solutions for $T_q(t)$ given an initial pulse $T_q^{(ext)}(0)$ at a specific wave vector \mathbf{q} , are,

$$T_q(t) = T_q^{(ext)}(0) \frac{e^{-\frac{t}{2\tau_{ss}}} \cos(\beta t - \phi)}{\cos \phi}, \quad (9)$$

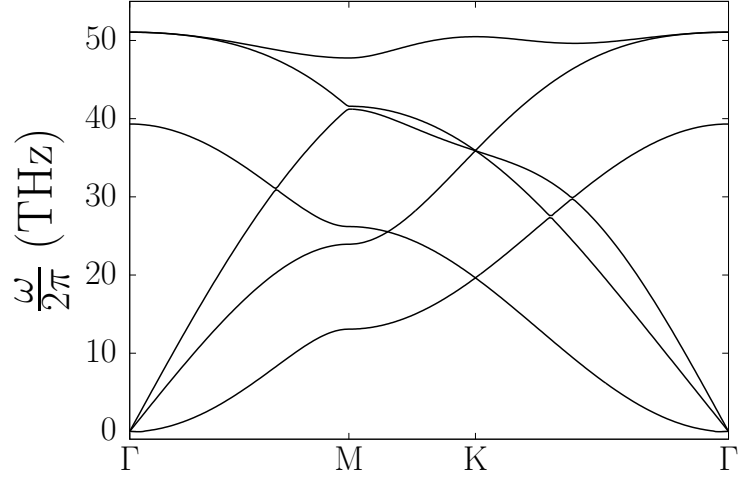


Figure 7: Computed phonon band structure for the optimized Tersoff potential [14].

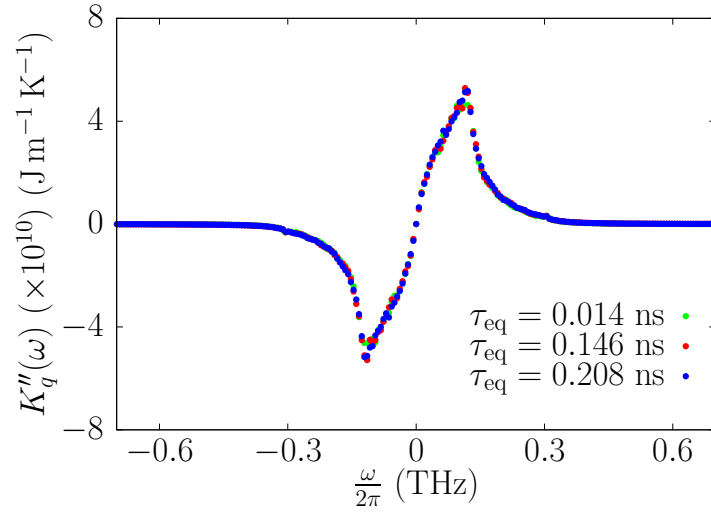


Figure 8: Response function $K_q''(\omega)$ for $q = q_1 = \frac{2\pi}{L}$ obtained from data sets corresponding to the three different times τ_{eq} for the equilibration step. This plot demonstrates that results are not sensitive to τ_{eq} .

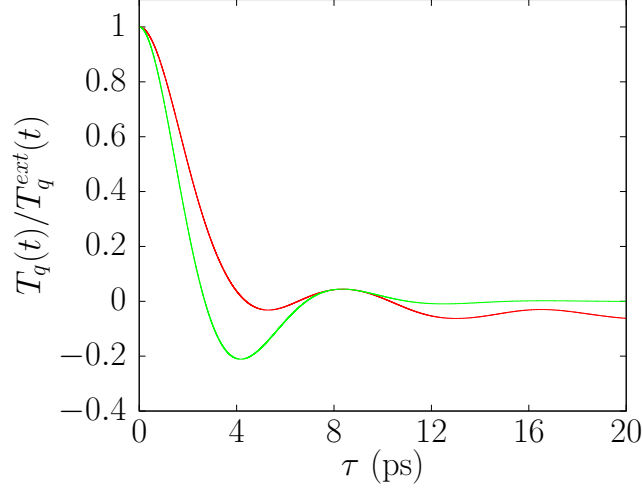


Figure 9: Fit to Eq. 9

in which the oscillation frequency $\beta = \sqrt{\omega_q^2 - \frac{1}{4\tau_{ss}^2}}$ and $\omega_q = v_{ss}q$. The angle ϕ is chosen so that $\frac{dT_q}{dt} = 0$ at $t = 0$ which corresponds exactly to the MD simulation results. Then for ϕ we have the expression,

$$\tan \phi = \frac{1}{2\beta\tau_{ss}}. \quad (10)$$

From the computed response functions $K_q(\tau)$, the Fourier component $T_q(t)$ due to an initial perturbation $T_q^{(ext)}(0)$ at $t = 0$ evolves according to,

$$T_q(t) = T_q^{(ext)}(0) \left(1 - \frac{q^2}{c_V} \int_0^t K_q(\tau) d\tau \right) \quad (11)$$

Using the results functions $K_q(\tau)$ plotted in Fig. 2, the quantity $1 - \frac{q^2}{c_V} \int_0^t K_q(\tau) d\tau$ can be computed as a function of the upper limit of integration, resulting in a prediction for $\frac{T_q(t)}{T_q^{(ext)}(0)}$, showing the oscillations and the decay of the input heat pulse. This quantity is shown for $q_1 = \frac{2\pi}{L}$ in Fig. 9. The curve is not very accurately described by Eq. 9. Instead of attempting to fit Eq. 9 directly to the simulation, we instead set the parameter β to give the oscillation period, and then adjusted τ_{ss} to exactly give the amplitude of the first peak. This “fit” is also shown in Fig. 9. This procedure was repeated for q_2 and q_3 , resulting in values for τ_{ss} and v_{ss} to determine trends which can be compared to experiment. These values are shown in Table 1.

The results in Table 1 show, perhaps not surprisingly, that v_{ss} depends only weakly on q , indicating approximately linear dispersion for second sound. This is despite the fact that, as has been shown, the second-sound pulse is comprised of the effect of many phonon branches, many not characterized by linear dispersion. The lifetime τ_{ss} does show significant dependence on q . As demonstrated below, the strong dependence of τ_{ss} on q is seen in experiment, but is not predicted by the BTE theory of second sound.

The values in Table 1 can be compared to experimental TTG results for graphite [2]. In that work, grating periods in the range from $4 - 16 \mu\text{m}$ result in second sound speeds v_{ss} in the range between $3 - 4 \text{ km s}^{-1}$, which is somewhat smaller than our values in Table 1. The trend in Ref. [2] is for v_{ss} to increase as the grating period decreases, especially for values below $\sim 3 \mu\text{m}$. However, experimental values for v_{ss} vary by less than a factor of 2 for grating periods from $3 - 15 \mu\text{m}$.

Table 1: Resulting parameters v_{ss} and τ_{ss} obtained from fitting simulation results to Eq. 9 as described in the text. The simulation data and fit curve for q_1 are both shown in Fig. 9. Also included is the coherent propagation length $\lambda_{ss} = 2v_{ss}\tau_{ss}$. The length scale $L = 68.1\text{nm}$ for the MD simulations.

$ q $	v_{ss} (km s ⁻¹)	τ_{ss} (ps)	$\lambda_{ss} = 2v_{ss}\tau_{ss}$ (μm)
$q_1 = \frac{2\pi}{L}$	9.12	1.34	0.024
$q_2 = \frac{4\pi}{L}$	8.69	0.96	0.016
$q_3 = \frac{6\pi}{L}$	8.68	0.68	0.011

However, the trend of increasing v_{ss} with decreasing grating period is broadly consistent with the larger values for v_{ss} for the length scales simulated here.

The lifetime τ_{ss} is reported for experimental results with graphite samples in Ref. [2]. Specifically, Ref. [2] reports propagation lengths λ_{ss} , defined by $\lambda_{ss} = 2v_{ss}\tau_{ss}$, which appear to approach zero as the grating period approaches zero, and saturate at large grating periods to $\lambda_{ss} \sim 2\mu\text{m}$. Hence, for grating periods below $\sim 4\mu\text{m}$, experiment shows that τ_{ss} is strongly dependent on grating period. This is qualitatively consistent with the simulation data in Table 1, although admittedly simulation results were obtained for much smaller length scales. For the smallest grating period $2\mu\text{m}$ used in the experiment, the value for τ_{ss} can be estimated from the data in Ref. [2] to be $\sim 20\text{ps}$. This τ_{ss} is larger than those in Table 1, but the trend is reasonable given the larger length scale in the experiment.

Many studies of second sound have been based on solutions to the BTE. Early work by Enz [4] classified second sound as either “drifting” or “driftless”. Later, Hardy [5] used the phonon BTE and showed that so-called drifting second sound requires normal scattering to dominate over Umklapp scattering, so that rapidly a drifting distribution is established. This condition is generally understood to be realized in two-dimensional materials like graphene and is closely connected to both phonon hydrodynamics and second sound [6, 7]. In Ref. [7], the BTE was solved in the Callaway approximation to the single-mode relaxation time approximation,

$$\sum_{\nu_2} \Omega_{\nu_1, \nu_2} n_{\nu_2} = -\frac{n_{\nu} - n_{\nu}^{drift}}{\tau_{\nu_1}^N} - \frac{n_{\nu} - \bar{n}_{\nu}}{\tau_{\nu_1}^R}, \quad (12)$$

in which $\nu_1 = (\mathbf{k}_1, s_1)$ and $\nu_2 = (\mathbf{k}_2, s_2)$, and Ω_{ν_1, ν_2} is the phonon scattering matrix. The distribution $\bar{n}_{\nu}(T_0)$ is the usual Bose-Einstein function applied to each mode ν . The drifted distribution is given by,

$$n_{\nu}^{drift} = [e^{\beta(\hbar\omega_{\mathbf{k},s} - \hbar\mathbf{q}\cdot\mathbf{V})} - 1]^{-1} \quad (13)$$

in which $\mathbf{q}\cdot\mathbf{V}$ represents a shift in the distribution which results from dominance of the momentum-conserving normal scattering. Using these approximations and also the continuity equation, the second-sound equation was derived in Ref. [6, 7], with expressions for v_{ss} and τ_{ss} . Specifically, for an isotropic medium, these were shown to be,

$$v_{ss}^2 = \frac{\frac{1}{2} \sum_{\nu} C_{\nu} \mathbf{v}_{\nu} \cdot \mathbf{v}_{\nu}}{\sum_{\nu} C_{\nu}} \quad (14)$$

$$\frac{1}{\tau_{ss}} = \frac{\sum_{\nu} \frac{C_{\nu} q^i v_{\nu}^i}{\omega_{\nu} \tau_{\nu}^R}}{\sum_{\nu} \frac{C_{\nu} q^i v_{\nu}^i}{\omega_{\nu}}}, \quad (15)$$

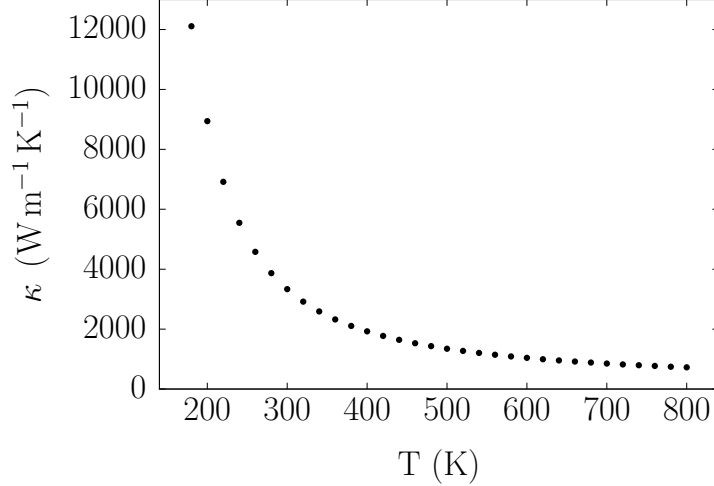


Figure 10: Graphene thermal conductivity κ vs. temperature T obtained from solutions of the LBTE.

in which v_v^i and q^i represent components of vectors Cartesian direction indicated by the superscript. It should be noted that here q^i represents a component of the “drifted” distribution in momentum space, and does not specifically refer a Fourier component of any excitation. Hence, despite the presence of q^i in Eq. 15, in fact the value of τ_{ss} is in fact independent of the specific value of q^i . The scattering times τ_v^R are obtained from the imaginary part of the self-energy function specifically related to Umklapp scattering process. In Ref. [7], this approach resulted in the predictions for graphene $\tau_{ss} \sim 100 - 200$ ps and propagation lengths $\lambda_{ss} = 2v_{ss}\tau_{ss} \sim 2\mu\text{m}$ at $T = 300\text{K}$ [7]. Note that the definition of λ_{ss} in Ref. [7] differs by a factor of 2 from the one used here, which was chosen to agree with the definition in Ref. [2]. It is clear from Eq. 15 that τ_{ss} depends on the resistive, Umklapp scattering rate τ_v^R , weighted over all of the phonon modes $v = (\mathbf{k}, s)$. In this picture then, it is only anharmonic scattering which causes decay of the drifting phonon distribution and the eventual dissipation of second sound.

Here we reproduce these results with our own calculations. We used the phono3py code [16,17] along with VASP for DFT calculations [19–22]. The system used was an 8×8 graphene supercell with 128 atoms. The mesh in reciprocal space was a $3 \times 3 \times 1$ Monkhorst-Pack type mesh. The C-C bond length used in the DFT calculations was 1.425\AA . Gaussian smearing was used for the Brillouin zone integration with a sigma value of $\sigma = 0.05$ eV. Thermal conductivity as a function of temperature T was obtained by solving the full LBTE using a $100 \times 100 \times 1$ reciprocal-space mesh with the tetrahedron method for Brillouin-zone integration. The results of these calculations are shown in Fig. 10. At room temperature, we obtained a value $\kappa = 3,348$ Wm/K, which can be compared to the results of other authors. Specifically, also using VASP and the same reciprocal-space grid, Ref. [30] reports a room-temperature result $\kappa \approx 2,870$ W/mK at 300K. However, this result included isotopic scattering which likely accounts for their lower κ value. In Ref. [7], the LBTE was solve with a $128 \times 128 \times 1$ mesh and Gaussian smearing of 10 cm^{-1} . This work reports $\kappa \approx 4000\text{W/mK}$ near 300K which is comparable although slightly higher than our result.

Having established the general validity of the DFT results, we next computed v_{ss} and τ_{ss} using the expressions in Eqs. 14-15. Our calculated values of v_{ss} and τ_{ss} are 6.6 km/s and 50 ps resulting in a propagation length $\lambda_{ss} = 2v_{ss}\tau_{ss} = 0.66\mu\text{m}$. For comparison, Ref. [7] reports a comparable value for $v_{ss} \sim 6.5 \text{ km/s}$, but the somewhat larger value $\tau_{ss} \sim 150 \text{ ps}$. This leads to the propagation length $\lambda_{ss} \sim 2\mu\text{m}$. While these results are not in exact agreement, for reasons that are not immediately

clear, they both result in propagation lengths λ_{ss} at micron scales near room temperature.

From the analysis above, appears the BTE theory of second sound is in rather stark contrast with experiment and MD simulation results here for graphene and previously for hBN [13]. First, values for τ_{ss} from BTE theory tend to be very large in comparison to MD simulation, and moreover are entirely independent of \mathbf{q} . In Table 1, values for λ_{ss} from the MD simulations are reported. These values are clearly much smaller than $\lambda_{ss} = 0.66\mu\text{m}$ obtained from our BTE calculations. As noted elsewhere, TTG experiments on graphite demonstrate that τ_{ss} is strongly dependent on the grating period [2], which is entirely inconsistent with the BTE theory. These observations point towards the importance of phonon dispersion and loss of wave coherence as being the dominant mechanism for second-sound dissipation when length scales at short length scales and relatively low temperature. However, at longer length scales and higher temperatures, where second sound is less likely to be observed, the BTE theory is more likely to be applicable. For example, the experimental results for graphite [2] show that τ_{ss} saturates to a constant value at grating periods beyond $\sim 10\mu\text{m}$.

5 Time-dependent sources

In this section we elucidate second sound generated by time-dependent sources. We note that TTG studies generally involve a single pulse with short time duration occurring at a single wave vector \mathbf{q} to describe the grating period. However, at least in principle, these excitations could be made to be time-dependent. In our original work [11] we briefly discussed the response to time-dependent sources. Here the physics is elucidated in more detail, including predictions of where second sound might be either enhanced or suppressed by changing the frequency ω of the excitation source for a specific \mathbf{q} . The main physical consideration here is the observation that the heat-current lags the excitation which generated it, and as a result, the transport is always out of phase with the excitation. This is in direct contrast to Fourier's law, where the current response is instantaneous.

Here we consider an excitation source given by,

$$H^{(ext)}(\mathbf{r}, t) = \frac{1}{4}H_0 (e^{i\mathbf{q}\cdot\mathbf{r}} + e^{-i\mathbf{q}\cdot\mathbf{r}}) (e^{i\omega t} + e^{-i\omega t}) = H_0 \cos(\mathbf{q} \cdot \mathbf{r}) \cos(\omega t) \quad (16)$$

Then following Ref. [11], the time-dependent temperature field, including the effect of the heating source, is given by,

$$T(\mathbf{r}, t) = T_0 + \frac{H_0^{(ext)}}{c_V \omega} \left[\left(1 - \frac{q^2}{c_V} K'_q(\omega) \right) \sin \omega t + \frac{q^2}{c_V} K''_q(\omega) \cos \omega t \right] \cos(\mathbf{q} \cdot \mathbf{r}) \quad (17)$$

It is also useful to write this expression in a different form that shows the phase difference between the heating source and the temperature response,

$$T(\mathbf{r}, t) = T_0 + \frac{H_0^{(ext)}}{c_V \omega} \left[\sin \omega t - \frac{q^2}{c_V} |\tilde{K}_q(\omega)| \sin(\omega t - \delta) \right] \cos(\mathbf{q} \cdot \mathbf{r}), \quad (18)$$

in which $|\tilde{K}_q(\omega)| = \sqrt{K_q'^2(\omega) + K_q''^2(\omega)}$ is the magnitude of the response function and the phase angle is given by,

$$\tan \delta = \frac{K_q''(\omega)}{K_q'(\omega)} \quad (19)$$

Both the magnitude of the response function and the phase angle are therefore functions of the source frequency ω . It can be inferred that the oscillatory temperature tends to be damped most

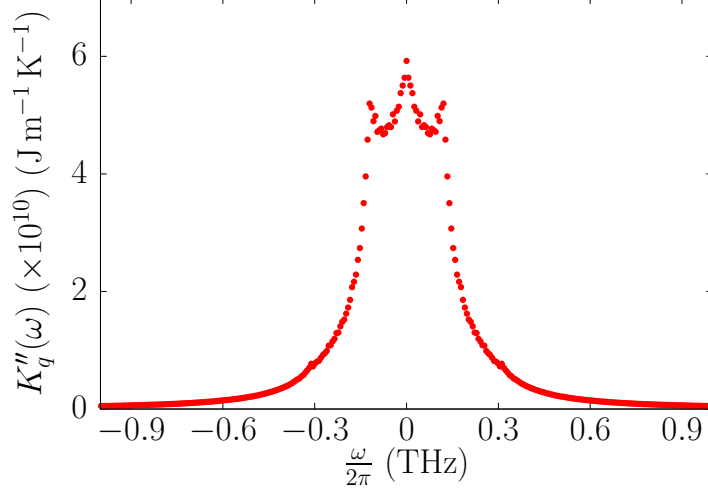


Figure 11: Magnitude of the response function $|\tilde{K}_q(\omega)|$ for $q = q_1 = \frac{2\pi}{L}$.

strongly when K'_q is large and K''_q is relatively small, since then the response is large and in-phase with the temperature fluctuations due to the source.

In Fig. 11, the magnitude $|\tilde{K}_q(\omega)|$ of the response function is plotted. In Fig. 12, the phase angle $\delta = \arctan\left(\frac{K''_q}{K'_q}\right)$ is shown as a function of frequency ω . Not surprisingly, the magnitude is largest at the maximum of $K'(\omega)$, which occurs at $\omega = 0$, and also at the maxima of $K''_q(\omega)$. For very small driving frequencies, the normal-modes are able to keep up with the perturbation, and dissipation of the excitation is maximized. Further away from $\omega = 0$, the phase angle becomes an important factor, tending to admit larger-amplitude temperature deviations. For ω very near the peak of $K''_q(\omega)$, the phase angle tends to $\delta = \pm\frac{\pi}{2}$, and Eq. 18 shows that the temperature response is maximally out of phase with the source. Finally, for frequencies outside of the range $\pm 0.3\text{THz}$, the normal modes are not able to keep up and are ineffective at dissipating the perturbation. This could have significant implications for time-dependent sources, and moreover demonstrates how time-dependent sources could be used to probe the second-sound spectra to validate theoretical predictions.

For completeness, we also give the above evolution equation for $T(\mathbf{r}, t)$ using the response function from the heat-diffusion equation,

$$T(\mathbf{r}, t) = T_0 + \frac{H_0^{(ext)}}{\kappa C_V} \left[K'_q(\omega) \cos \omega t + K''_q(\omega) \sin \omega t \right] \cos(\mathbf{q} \cdot \mathbf{r}) . \quad (20)$$

This form appears different but in fact is equivalent to what was derived in Ref. [11]. It is also interesting to note that the relationship between the $K'_q(\omega)$ and $K''_q(\omega)$ terms and the $\sin \omega t$ and $\cos \omega t$ terms. This arises because in Fourier's law, the current response occurs immediately when the heat pulse is input, whereas the MD simulations and the computed response functions show that the current response lags behind the input heat pulse.

6 Discussion and Conclusions

In this paper we have presented MD simulation results for thermal transport in single-layer graphene at length scales up to $\sim 68.1\text{nm}$. The results demonstrate second sound and strong deviations from Fourier's law at all simulated scales for $T = 300\text{K}$. This is very consistent with our prior study of

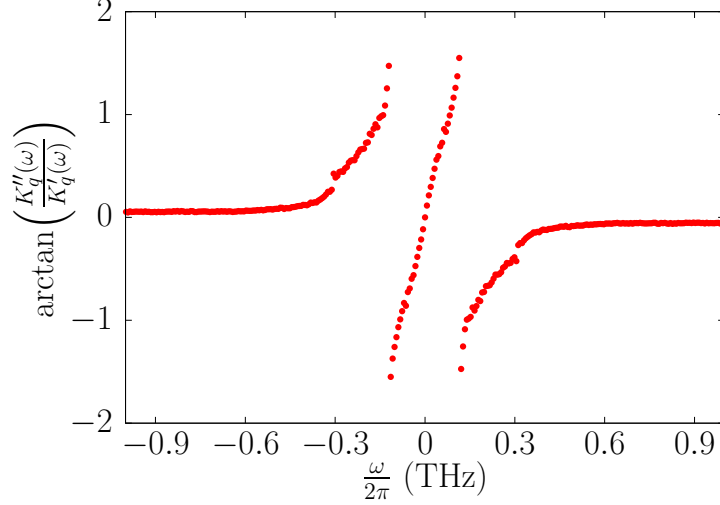


Figure 12: Phase angle $\delta = \arctan\left(\frac{K''_q(\omega)}{K'_q(\omega)}\right)$.

hBN where second sound was clearly observed at scales up to 110.8nm for $T = 100\text{K}$ [13]. In both of these systems, the limiting values of temperature and length scale where second sound might be observed has not been fully established either theoretically or in experiment.

An important result is that the lifetime of second sound τ_{ss} is strongly dependent on the wave vector \mathbf{q} of the temperature deviation. This is in contradiction to predictions based on BTE theories of second sound, which predict τ_{ss} is primarily dependent on anharmonic scattering rates and is independent on the vector \mathbf{q} characterizing a perturbation. Our predictions appear to be in agreement with TTG experimental results for graphite, where τ_{ss} is shown to be strongly dependent on the grating period below $10\mu\text{m}$ [1, 2]. For very large grating periods ($> 10\mu\text{m}$), τ_{ss} determined experimentally appears to saturate, which is characteristic of diffusive transport [1, 2].

For short length scales and low temperatures, our results show that coherent second sound depends strongly on phonon dispersion. In essence, a source, for example in a TTG experiment with a grating period characterized by \mathbf{q} , generates coherent phonon wave packets which tend to spread over time and result in decay of the second-sound wave. Anharmonic scattering is still present and plays a role, eventually becoming the dominant dissipation mechanism at longer length scales and higher temperatures. It is also important to note that second sound decay, when dominated by phonon dispersion, does not mean that subsequent transport is diffusive. Specifically, phonon dispersion results in a loss of phase coherence which can occur on timescales much shorter than the anharmonic scattering times. Hence, second sound requires ballistic transport, but an absence of a clear evidence of second sound does not necessarily indicate diffusive transport. Ballistic transport may be important even when second sound cannot be observed. These points were also made in our previous study of hBN [13].

As noted in our previous study of hBN, sharp spectral features may emerge in connection with resonant behavior in a particular band characterized by linear dispersion [13]. Sometimes in the literature these features are referred to as “first sound”. However, in the physical picture developed here, these sharp features in the response function spectra $\tilde{K}_q(\omega)$ correspond to excitations which are not distinct from what we call “second sound”. What might occur under certain conditions is that very specific phonon branches may be resonantly excited and propagate at a sufficient velocity to be detected independently from the “thermal” second sound. For example, in our hBN paper [13], even at the very high temperature $T = 1200\text{K}$, distinct, coherent modes from the

longitudinal-acoustic branch (LA) were observed in the calculations even when the second sound signal was essentially undetectable. In the present study of graphene, such sharp features are not as clearly apparent, but may be more noticeable at different length scales, temperatures, or strain conditions.

The relatively weak second-sound signal observed in our calculations, in contrast to experiments in graphite, most likely results primarily from two considerations. First, in graphite, it has been observed that the parabolic ZA branch tends to become more linear in comparison to monolayer graphene. In the physical picture provided here, linear dispersion results in stronger resonance in second sound propagation via the ZA branch, and hence a longer lifetime. Second, quantum statistics results in occupation of low-frequency acoustic modes, with higher-frequency optical modes unoccupied at low temperature. By contrast, our classical simulations result in contributions across the entire spectrum. Hence, classical MD simulations should result in a broader spectrum for $\tilde{K}_{\mathbf{q}}(\omega)$, and therefore a shorter lifetime for second sound propagation. More accurate predictions will emerge from theory that can account for quantum statistics.

The approach presented here to predict the response due to time-dependent sources has implications for experimental methods to elucidate second-sound spectra. Specifically, time-dependent experiments, possibly using TTG techniques, might be used to probe the spectral response. It was shown that both the magnitude of the response function and the phase angle between the source and response can be connected in a simple way to the observed temperature oscillations. This might be a way to directly probe second sound spectra to validate some of our predictions.

We also note that there have been time-dependent BTE methods developed which have similar objectives, namely to elucidate the response to time-dependent sources [23,24]. For example, the reported results for graphite were analyzed with this approach [24]. It appears that there may be connections between the time-dependent BTE approaches and response functions. However, we have not yet tried to elucidate the relationships between these approaches. We do note that Ref. [24] does lead to strong spectral response at frequencies $\omega \sim \pm \mathbf{q} \cdot \mathbf{v}_{\mathbf{k},s}$, which is also present in the first-principles theory in our previous paper [13] and described qualitatively in our analysis of the spectral response presented here.

Finally, in our previous paper [13], we outlined how the response functions approach might be approached to be fully quantum-mechanical and use first-principles DFT calculations. The theory developed has connections with much earlier work by Sham [25,26]. It is currently our objective to apply this methodology using the large dataset for graphene that we have used to compute thermal conductivity κ using solutions to the LBTE. It is expected that correct quantum statistics will result in a more narrow spectral response, for the reasons argued above, and hence longer lifetimes

τ_{ss} .

References

- [1] S. Huberman, R. A. Duncan, K. Chen, B. Song, V. Chiloyan, Z. Ding, A. A. Maznev, G. Chen, and K. A. Nelson. Observation of second sound in graphite at temperatures above 100k. *Science*, 364(6438):375–379, 2019.
- [2] Zhiwei Ding, Ke Chen, Bai Song, Jungwoo Shin, Alexei A. Maznev, Keith A. Nelson, and Gang Chen. Observation of second sound in graphite over 200k. *Nature Communications*, 13(1):285, 2022.
- [3] Nicola Bonini, Jivtesh Garg, and Nicola Marzari. Acoustic phonon lifetimes and thermal transport in free-standing and strained graphene. *Nano Letters*, 12(6):2673–2678, may 2012.
- [4] Charles P Enz. One-particle densities, thermal propagation, and second sound in dielectric crystals. *Annals of Physics*, 46(1):114–173, 1968.
- [5] Robert J. Hardy. Phonon boltzmann equation and second sound in solids. *Physical Review B*, 2(4):1193–1207, 1970.
- [6] Sangyeop Lee, David Broido, Keivan Esfarjani, and Gang Chen. Hydrodynamic phonon transport in suspended graphene. *Nature Communications*, 6(1), February 2015.
- [7] Andrea Cepellotti, Giorgia Fugallo, Lorenzo Paulatto, Michele Lazzeri, Francesco Mauri, and Nicola Marzari. Phonon hydrodynamics in two-dimensional materials. *Nature Communications*, 6(1):6400, 2015.
- [8] Sangyeop Lee and Lucas Lindsay. Hydrodynamic phonon drift and second sound in a (20,20) single-wall carbon nanotube. *Physical Review B*, 95(18):184304, 2017.
- [9] Xiao-Ping Luo and Yang-Yu Guo, Mo-Ran Wang, and Hong-Liang Yi. Direct simulation of second sound in graphene by solving the phonon boltzmann equation via a multiscale scheme. *Physical Review B*, 100(15):155401, 2019.
- [10] Man-Yu Shang, Wen-Hao Mao, Nuo Yang, Baowen Li, and Jing-Tao Lu. Unified theory of second sound in two-dimensional materials. *Physical Review B*, 105(16):165423, 2022.
- [11] Kevin M. Fernando and Patrick K. Schelling. Non-local linear-response functions for thermal transport computed with equilibrium molecular-dynamics simulation. *Journal of Applied Physics*, 128(21):215105, 2020.
- [12] Nathaniel Bohm and Patrick K. Schelling. Analysis of ballistic transport and resonance in the alpha-fermi-pasta-ulam-tsingou model. *Phys. Rev. E*, 106:024212, Aug 2022.
- [13] Patrick K. Schelling. Thermal response functions and second sound in single-layer hexagonal boron nitride. *Physical Review B*, 112(2), 2025.
- [14] L. Lindsay and D. A. Broido. Optimized tersoff and brenner empirical potential parameters for lattice dynamics and phonon thermal transport in carbon nanotubes and graphene. *Physical Review B*, 81(20):205441, 2010.
- [15] Zheyong Fan, Luiz Felipe C. Pereira, Hui-Qiong Wang, Jin-Cheng Zheng, Davide Donadio, and Ari Harju. Force and heat current formulas for many-body potentials in molecular dynamics simulations with applications to thermal conductivity calculations. *Physical Review B*, 92(9):094301, 2015.

- [16] Atsushi Togo, Laurent Chaput, Terumasa Tadano, and Isao Tanaka. Implementation strategies in phonopy and phono3py. *Journal of Physics: Condensed Matter*, 35(35):353001, 2023.
- [17] Atsushi Togo. First-principles phonon calculations with phonopy and phono3py. *Journal of the Physical Society of Japan*, 92(1), January 2023.
- [18] Robert J. Hardy. Energy-flux operator for a lattice. *Physical Review*, 132(1):168–177, 1963.
- [19] G Kresse and J Hafner. Norm-conserving and ultrasoft pseudopotentials for first-row and transition elements. *Journal of Physics: Condensed Matter*, 6(40):8245–8257, October 1994.
- [20] G. Kresse and J. Furthmüller. Efficiency of ab-initio total energy calculations for metals and semiconductors using a plane-wave basis set. *Computational Materials Science*, 6(1):15–50, 1996.
- [21] G. Kresse. From ultrasoft pseudopotentials to the projector augmented-wave method. *Physical Review B*, 59(3):1758–1775, 1999.
- [22] G. Kresse and J. Furthmüller. Efficient iterative schemes for ab initio total-energy calculations using a plane-wave basis set. *Phys. Rev. B*, 54:11169–11186, Oct 1996.
- [23] Chengyun Hua and Lucas Lindsay. Space-time dependent thermal conductivity in nonlocal thermal transport. *Physical Review B*, 102(10):104310, 2020.
- [24] Vazrik Chiloyan. Green’s functions of the boltzmann transport equation with the full scattering matrix for phonon nanoscale transport beyond the relaxation-time approximation. *Physical Review B*, 104(24), 2021.
- [25] L. J. Sham. Equilibrium approach to second sound in solids. *Physical Review*, 156(2):494–500, 1967.
- [26] L. J. Sham. Temperature propagation in anharmonic solids. *Physical Review*, 163(2):401–407, 1967.
- [27] X. Xu, L. F. C. Pereira, Y. Wang, J. Wu, K. Zhang, X. Zhao, S. Bae, C. Tinh Bui, R. Xie, J. T. L. Thong, B. H. Hong, K. P. Loh, D. Donadio, B. Li, and B. Özyilmaz. Length-dependent thermal conductivity in suspended single-layer graphene. *Nature Communications*, 5(1):3689, April 2014.
- [28] J. Haskins, A. Kımacı, C. Sevik, H. Sevinçli, G. Cuniberti, and T. Çağın. Control of Thermal and Electronic Transport in Defect-Engineered Graphene Nanoribbons. *ACS Nano*, 5(5):3779–3787, May 2011.
- [29] W. Cai, A. L. Moore, Y. Zhu, X. Li, S. Chen, L. Shi, and R. S. Ruoff. Thermal Transport in Suspended and Supported Monolayer Graphene Grown by Chemical Vapor Deposition. *Nano Letters*, 10(5):1645–1651, May 2010.
- [30] S. Han, D. Lee, S. Lee, G.-D. Lee, S. Lee, and H. Jang. Lattice thermal conductivity and phonon transport properties of monolayer fluorographene. *Journal of Applied Physics*, 136(13):134305, 2024.